Publication Year	2020
Acceptance in OA @INAF	2022-02-08T15:03:24Z
Title	þÿ Q u a s i - p e r i o d i c b e h a v i o u r i n t h e o p t i c a l a n d ³ - r a y l i g h and B2 1633+38
Authors	Otero-Santos, J.; Acosta-Pulido, J. A.; Becerra González, J.; RAITERI, Claudia Maria; Larionov, V. M.; et al.
DOI	10.1093/mnras/staa134
Handle	http://hdl.handle.net/20.500.12386/31366
Journal	MONTHLY NOTICES OF THE ROYAL ASTRONOMICAL SOCIETY
Number	492

Quasi-periodic behaviour in the optical and γ-ray light curves of blazars 3C 66A and B2 1633+38

J. Otero-Santos [1,2]★ J. A. Acosta-Pulido,[1,2]★ J. Becerra González,[1,2]★ C. M. Raiteri [3]
V. M. Larionov [4,5] P. Peñil,[6] P. S. Smith,[7] C. Ballester Niebla,[8] G. A. Borman,[9]
M. I. Carnerero,[3] N. Castro Segura,[2,10] T. S. Grishina,[4] E. N. Kopatskaya,[4]
E. G. Larionova,[4] D. A. Morozova,[4] A. A. Nikiforova,[4,5] S. S. Savchenko,[4]
Yu. V. Troitskaya,[4] I. S. Troitsky,[4] A. A. Vasilyev[4] and M. Villata[3]

[1]*Instituto de Astrofísica de Canarias (IAC), E-38200 La Laguna, Tenerife, Spain*
[2]*Departamento de Astrofísica, Universidad de La Laguna (ULL), E-38206 La Laguna, Tenerife, Spain*
[3]*INAF-Osservatorio Astrofisico di Torino, via Osservatorio 20, I-10025 Pino Torinese, Italy*
[4]*Astronomical Institute, St Petersburg State University, Universitetskij Pr. 28, Petrodvorets, 198504 St Petersburg, Russia*
[5]*Pulkovo Astronomical Observatory of RAS, Pulkovskoye shosse 60, 196149 St Petersburg, Russia*
[6]*IPARCOS and Department of EMFTEL, Universidad Complutense de Madrid, E-28040 Madrid, Spain*
[7]*Steward Observatory, University of Arizona, Tucson, AZ 85721, USA*
[8]*Facultad de Ciencias, Universidad de La Laguna (ULL), E-38206 La Laguna, Tenerife, Spain*
[9]*Crimean Astrophysical Observatory, P/O Nauchny, 298409 Crimea*
[10]*School of Physics & Astronomy, University of Southampton, Highfield, SO17 1BJ Southampton, UK*

ABSTRACT

We report on quasi-periodic variability found in two blazars included in the Steward Observatory Blazar Monitoring data sample: the BL Lac object 3C 66A and the Flat Spectrum Radio Quasar B2 1633+38. We collect optical photometric and polarimetric data in *V* and *R* bands of these sources from different observatories: St. Petersburg University, Crimean Astrophysical Observatory, WEBT–GASP, Catalina Real-Time Transient Survey, Steward Observatory, STELLA Robotic Observatory, and Katzman Automatic Imaging Telescope. In addition, an analysis of the γ-ray light curves from *Fermi*–LAT is included. Three methods are used to search for any periodic behaviour in the data: the Z-transform Discrete Correlation Function, the Lomb–Scargle periodogram and the Weighted Wavelet Z-transform. We find pieces of evidence of possible quasi-periodic variability in the optical photometric data of both sources with periods of ∼3 yr for 3C 66A and ∼1.9 yr for B2 1633+38, with significances between 3σ and 5σ. Only B2 1633+38 shows evidence of this behaviour in the optical polarized data set at a confidence level of 2σ–4σ. This is the first reported evidence of quasi-periodic behaviour in the optical light curve of B2 1633+38. Also, a hint of quasi-periodic behaviour is found in the γ-ray light curve of B2 1633+38 with a confidence level $\geq 2\sigma$, while no periodicity is observed for 3C 66A in this energy range. We propose different jet emission models that could explain the quasi-periodic variability and the differences found between these two sources.

Key words: galaxies: active – BL Lacertae objects: general – BL Lacertae objects: individual (3C 66A, B2 1633+38) – galaxies: nuclei.

1 INTRODUCTION

Blazars are a subclass of active galactic nuclei (AGNs) whose jets closely point to the Earth, characterized by strong flux variability at different time-scales and high radio and optical polarization. These objects emit throughout the electromagnetic spectrum, from radio to γ-rays, showing a spectral energy distribution (SED) with

★ E-mail: jorge.otero.santos@gmail.com (JOS); jose.acosta@iac.es (JAAP); jbecerragonzalez@gmail.com (JBG)

a characteristic double bump structure (see e.g. Romero et al. 2017). Blazars can be categorized in two different classes (Urry & Padovani 1995): BL Lac objects and flat spectrum radio quasars (FSRQs). The differences between them rely on their optical spectra, (almost) featureless in the case of BL Lacs and with an emission-line equivalent width of $EW < 5\,\text{Å}$ (Böttcher 2019), the SED peak positions, and the Compton dominance (luminosity relation between the first and the second peak of the SED, see e.g. Finke 2013).

Blazars can show variability on a wide range of time-scales (see e.g. Fan et al. 2018; Gupta 2018): Intraday variability refers to changes on the order of minutes or hours. Short-term variability involves changes on time-scales of days to weeks. Finally, long-term variability concerns variations over time-scales of months to years. Various studies have searched for periodicity patterns on large time-scales in blazars as, e.g. Hovatta et al. (2007), Sandrinelli et al. (2016), Zhang et al. (2017a,b), and Fan et al. (2018). The detection of periodicity in blazars can have important implications for blazar emission models. Periodic behaviour can be interpreted within scenarios such as the presence of a supermassive binary black hole (SBBH, see e.g. Lehto & Valtonen 1996; Villata & Raiteri 1999), periodic changes in the jet emission mechanism like a helical jet (Lainela et al. 1999; Liu et al. 2010), helical structures, recurrent shock front formation, and/or disc instabilities (Marscher & Gear 1985; Camenzind & Krockenberger 1992; Tchekhovskoy, Narayan & McKinney 2011). Thus, the study of periodicity is fundamental to understand the processes taking place in the jets and accretion discs of black holes in active galaxies.

In this work, we analyse two sources, 3C 66A (also known as 3FGL J0222.6+4301) and B2 1633+38 (also known as 3FGL J1635.2+3809, 4C 38.41). These two objects were selected among a list of 27 sources observed by the Steward observatory[1] program in support of the *Fermi* γ-ray observations (from years 2008 to 2018). Twelve targets having more than 25 optical measurements per year were initially surveyed for periodicity. This preliminary examination for periodicity used the discrete correlation function (DCF) technique (Edelson & Krolik 1989) and 3C 66A and B2 1633+38 were selected since they exhibit a quasi-sinusoidal shape in their autocorrelation curve. Additional data from other observatories were gathered for these blazars, increasing the sampling to more than 200 observations per year. Note that objects showing evidence of periodic variability on longer time-scales, such as ∼12 yr for OJ 287 (Lehto & Valtonen 1996) will be missed in this search.

3C 66A is a BL Lac-type object classified as an intermediate synchrotron peaked blazar, according to its SED (Ackermann et al. 2015a). The redshift of this object is commonly referenced as $z = 0.444$ (Miller, French & Hawley 1978). Nevertheless, this value has been strongly questioned in several works (Finke et al. 2008; Furniss et al. 2013; Paiano et al. 2017; Torres-Zafra et al. 2018), since its spectrum does not show any emission line. Furniss et al. (2013) and Torres-Zafra et al. (2018) estimated a lower limit of the redshift of $z \geq 0.33$. 3C 66A has been the target of multiple monitoring campaigns and surveys, showing variability throughout the electromagnetic spectrum on multiple time-scales. It was detected by *Fermi–LAT* in high-energy (HE; $E > 100\,\text{MeV}$) γ-rays (Ackermann et al. 2016) and by VERITAS and the MAGIC telescopes in the very high-energy regime (VHE; $E > 100\,\text{GeV}$; Acciari et al. 2009; Aleksić et al. 2011). In the optical V and R bands, a period of 65 d was detected by Lainela et al. (1999), and

a period of 156 d was also detected by Fan et al. (2018), while different long-term analyses claimed periods of ∼2.5 yr (Belokon & Babadzhanyants 2003; Kaur et al. 2017) and ∼2 yr (Fan et al. 2018). Infrared intraday variability was also detected by de Diego et al. (1997), with significant spectral index variations associated. A variability on time-scales of hours was observed in X-rays by Ghosh & Soundararajaperumal (1995). The γ-ray variability properties were analysed by Vovk & Neronov (2013) with *Fermi–LAT* data. They found variations down to time-scales of ∼1.5 d. Intraday variability in radio wavelengths has also been studied by Liu et al. (2017), finding only marginal variations.

The other selected source, B2 1633+38, is a low synchrotron peaked source classified as an FSRQ, located at redshift $z = 1.814$ (Pâris et al. 2017). Strong flux variations were detected at optical wavelengths by Barbieri et al. (1977) in the B band. This was confirmed by Villata et al. (1997) with the analysis of intraday and short-term variability of the object in the R band. It has been observed throughout the spectrum (see e.g. Raiteri et al. 2012), finding hints of possible periods in radio wavelengths of ∼1.52 yr (Hovatta et al. 2007) and ∼3.07 yr (Fan et al. 2006). Moreover, Vovk & Neronov (2013) also found variations in the γ-ray flux of B2 1633+38 down to time-scales of ∼17 h.

In this paper, we study the long-term variability of these two blazars. We have large temporal coverage in the optical band, with light curves that span more than 9 yr in the different bands. This is an appropriate baseline for long-term periodicity studies and the identification of quasi-periodic oscillations on the order of a few years. This paper is structured as follows: in Section 2 the data sample and the reduction techniques are introduced, in Section 3 the different methods used in the periodicity analysis are described, and in Sections 4 and 5 we present and discuss the final results of the analysis for each source and the possible implications of these results. Finally, in Section 6 we end with a summary of the main results and provide possible interpretations.

2 OBSERVATIONS AND DATA REDUCTION

We have analysed optical and HE γ-ray *Fermi–LAT* data. Typically, γ-ray emission has been found correlated with the optical emission, so it is expected that periodicity found in the optical band may also show up in γ-rays (Bonning et al. 2009; Chatterjee et al. 2012; Liao et al. 2014; Carnerero et al. 2015; Rajput et al. 2019). Both optical photometric and polarimetric data were collected.

2.1 Optical data

2.1.1 Photometry

The long-term optical data used in this analysis have been obtained from several observatories and surveys, listed in Table 1. The GLAST-AGILE Support Program (GASP) of the Whole Earth Blazar Telescope[2] (WEBT; Villata et al. 2002, 2009) provided V- and R-band data for the two sources, which were taken during multiwavelength monitoring campaigns of 3C 66A in 2003–2004 (Böttcher et al. 2005) and 2007–2008 (Böttcher et al. 2009; Abdo et al. 2011), and of B2 1633+38 in 2008–2011 (Raiteri et al. 2012). Additional R-band data on 3C 66A come from the LX-200 0.4 m telescope from the St. Petersburg University and the AZT-8 0.7 m telescope from the Crimean Astrophysical Observatory (SPB and

Table 1. Long-term optical data sample for 3C 66A and B2 1633+38 from different observatories.

Source	Data base	Band	Monitoring epoch (UT)	Monitoring epoch (MJD)
3C 66A	St. Petersburg University & CrAO	R	2002 Feb. 17–2019 Oct. 31	52 323–58 788
	WEBT–GASP	R	2003 July 04–2009 Jan. 08	52 824–54 840
	WEBT–GASP	V	2007 July 20–2008 Mar. 03	54 301–54 529
	Catalina Real-Time Transient Survey (CRTS)	V	2008 Nov. 23–2013 Oct. 27	54 803–56 592
	Steward Observatory	R, V	2009 Sept. 14–2018 July 07	55 089–58 306
	Katzman Automatic Imaging Telescope (KAIT) monitoring	R	2010 Sept. 03–2018 Jan. 24	55 443–58 142
	STELLar Activity Robotic Observatory (STELLA)	R	2013 Dec. 03–2019 July 06	56 630–58 670
B2 1633+38	WEBT–GASP	R	2005 Mar. 15–2012 Jan. 30	53 445–55 956
	WEBT–GASP	V	2005 Mar. 15–2011 Oct. 22	53 444–55 856
	Catalina Real-Time Transient Survey (CRTS)	V	2005 May 06–2013 Oct. 15	53 557–56 580
	St. Petersburg University and CrAO	R	2005 July 09–2019 Oct. 01	53 560–58 757
	Steward Observatory	R, V	2008 Oct. 06–2018 July 07	54 745–58 306
	Katzman Automatic Imaging Telescope (KAIT) monitoring	R	2010 July 03–2018 July 29	55 380–58 328
	STELLar Activity Robotic Observatory (STELLA)	R	2014 July 31–2019 May 30	56 869–58 634

CrAO; Larionov et al. 2013). We also used the rich *V* and *R* data sets produced by the Steward Observatory program in support of the *Fermi* γ-ray observations[1] (Smith et al. 2009), and by the Catalina Real-Time Transient Survey[3] (CRTS; Drake et al. 2009) in *V* band. Finally, *R*-band data obtained by the Katzman Automatic Imaging Telescope[4] (KAIT; Li et al. 2003) and by the STELLar Activity Robotic Observatory[5] (STELLA; Strassmeier et al. 2004) were utilized. Retrieved data are already flux calibrated, with no need for further data reduction.

The *R*-band light curve of 3C 66A spans about 17.7 yr (MJD 52323–58788, 2002 February 17–2019 October 31), while the *V*-band data cover an interval of ~9.6 yr (MJD 54301–58306, 2007 July 20–2018 July 07). Both light curves are shown in Fig. 1. Due to big gaps and limited coverage of the *R*- and *V*-band light curves of 3C 66A, the data before MJD 52400 and MJD 55000, respectively, were not included in the periodicity analysis. The light curves of B2 1633+38 cover about 14.5 yr for the *R* band (MJD 53445–58757, 2005 March 15–2019 October 01) and 12.3 yr for the *V* band (MJD 53444–58306, 2005 March 15–2018 July 07). The resulting light curves are presented in Fig. 2. All the optical data were binned on a daily basis (taking the median value of all the values of each night) to perform the analysis in order to eliminate the errors and variations introduced by intraday variability. The calibration between different observatories was checked. All the calibrations were found to be consistent within uncertainties.

2.1.2 Polarimetry

We have also analysed the variability of the optical polarization in the *R* band. The data for both sources were retrieved from the ground-based Steward observatory *Fermi* support data base and the polarimetric observations of the St. Petersburg University made in St. Petersburg and the CrAO. The Steward *R*-band polarized data are obtained converting the total magnitude into polarized magnitude using the mean polarization degree in the 5000–7000 Å passband. The typical 1σ errors for the polarization degree are <1 per cent for the Steward Observatory data and <3 per cent for the St. Petersburg and CrAO data. The light curves corresponding to the polarimetric data are shown in Figs 1 and 2 for 3C 66A

and B2 1633+38, respectively. The polarized light curve of 3C 66A spans about 14 yr (MJD 53656–58756, 2005 October 13–2019 September 29). The polarized light curve of B2 1633+38 covers ~12 yr (MJD 54313–58729, 2007 August 01–2019 September 03). The polarimetric data were also binned on a daily basis to avoid effects due to intraday variability. The polarization degree has a relative variation with respect to the median of each night typically lower than a 10 per cent and 12 per cent for 3C 66A and B2 1633+38, respectively. Hagen-Thorn et al. (2019) found a scatter larger than the observational uncertainties in the rapid variation on the polarization of B2 1633+38. However, the change on the Stokes parameters shows roughly linear relations with the flux variations during the events. This permits to define an average polarization state for each event.

2.2 High-energy γ-rays: *Fermi–LAT* Data

The pair-conversion Large Area Telescope (LAT) on board the *Fermi* satellite monitors the γ-ray sky in survey mode every 3 h in the energy range from 20 MeV to >300 GeV (Atwood et al. 2009). For this work, a region of interest of 15° was selected centred around the two sources of interest, 3C 66A and B2 1633+382. The data sample included more than 10 yr of observations collected by *Fermi–LAT*, from 2008 August 04 to 2019 November 22 (MJD 54682-58809). The data reduction of the events of the Pass8 P8R3 source class was performed with the FERMITOOLS software package version 1.0.10 in the energy range 0.1–300 GeV. To reduce contamination from the limb of the Earth, a zenith angle cut of 90° was applied to the data. The likelihood fit of the data was performed using the recommended Galactic diffuse emission model and isotropic component recommended for the corresponding event selection used in this work.[6]
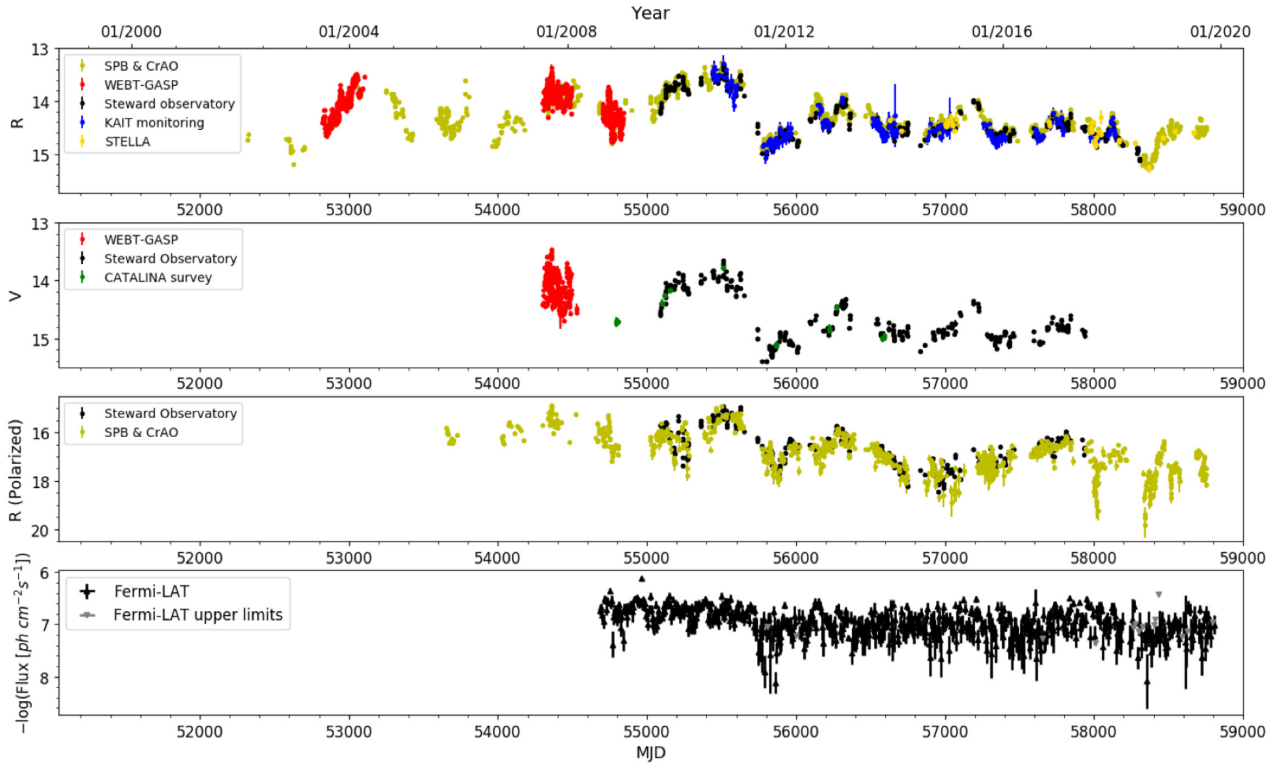
A first binned likelihood analysis was performed for the total integration range analysed within this work. The normalization of both diffuse components in the source model were allowed to freely vary during the spectral fitting. In addition to the source of interest, all the sources included in the 4FGL catalogue (The Fermi-LAT collaboration 2019) within a distance of 25° from the sources of interests were included. In the model, up to 15° distance, the targets spectral shape and normalization were left as free parameters, while they were fixed to their 4FGL catalogue values for sources located

[3]http://crts.caltech.edu/
[4]http://w.astro.berkeley.edu/bait/kait.html
[5]https://www.aip.de/en/research/facilities/stella/

[6]https://fermi.gsfc.nasa.gov/ssc/data/access/lat/BackgroundModels.html

Figure 1. Long-term light curves of 3C 66A. From top to bottom: Optical *R* band, Optical *V* band, Polarized magnitude in the optical *R* band, and *Fermi–LAT* γ-ray light curves. Different colours and symbols denote data from the different observatories used in the analysis.
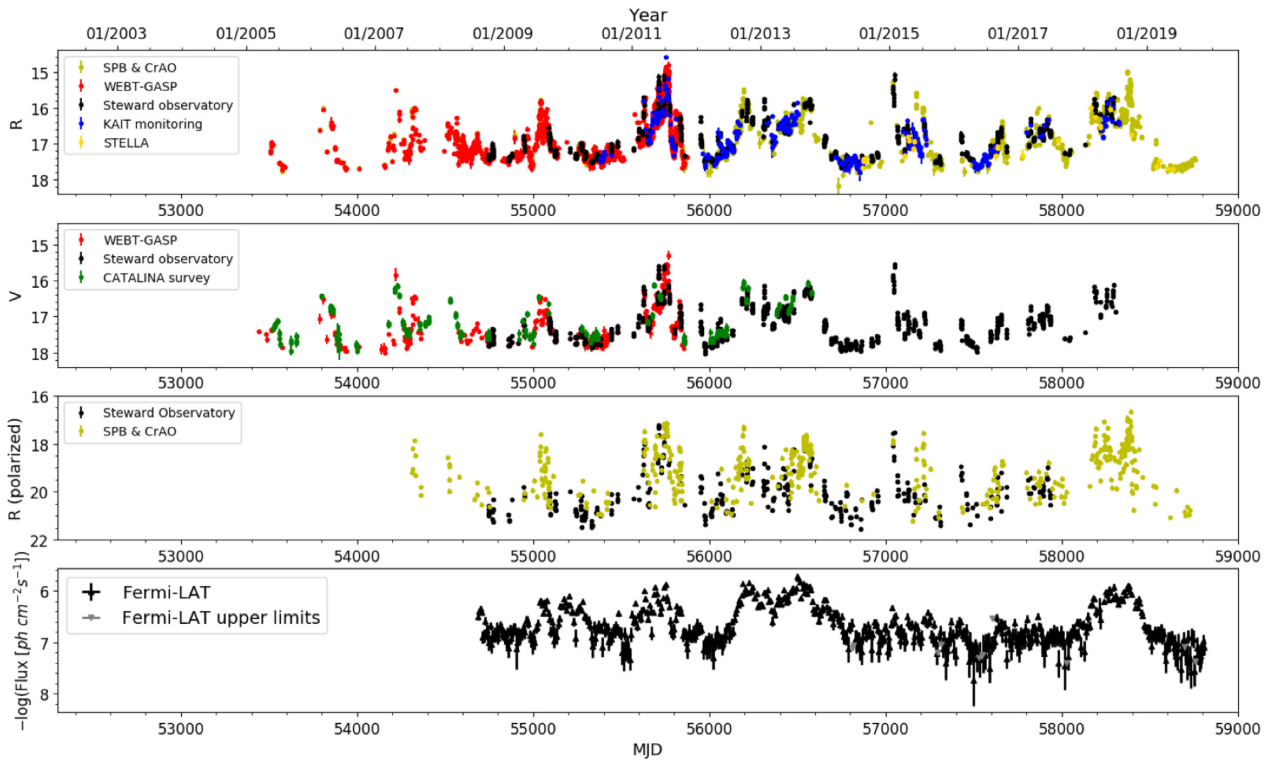
Figure 2. Long-term light curves of B2 1633+38. From top to bottom: Optical *R* band, Optical *V* band, Polarized magnitude in the optical *R* band, and *Fermi–LAT* γ-ray light curves. Different colours and symbols denote data from the different observatories used in the analysis.

between 15° and 25°. From this first fit all the sources located at a distance larger than 15° from the target of interest and with Test Statistic <2 were removed from the model. These simplified models were used for the calculation of the weekly binned light curves using an unbinned likelihood analysis for this short integration analysis. The resulting light curves are shown in Figs 1 and 2.

3 PERIODICITY ANALYSIS METHODS

Three different methods are used in this work to perform the periodicity analysis: the DCF, the Lomb–Scargle periodogram (LS), and the weighted wavelet Z-transform (WWZ). These methods were chosen due to their different approach when analysing the data. The DCF is optimized to find repeated patterns along the light curve despite the nature of the variation (e.g. flare-like events or sinusoidal variations). The LS periodogram decomposes the time series in sinusoidal components, and periodic signals are identified as peaks in the power spectral density (PSD). The WWZ works similarly as the LS, providing information about the periods of the signal and the time associated to those periods. The DCF works in time domain, while the other two work in the Fourier transformed domain.

3.1 Discrete correlation function

The DCF is commonly used in the study of AGNs and periodicity searches. While Fourier-based methods of unevenly sampled data can lead to interpolation and spurious peaks, along with another effects, the DCF is a robust method without interpolation in the temporal domain (Edelson & Krolik 1989). In this work, an improved DCF is used, named Z-Transformed DCF (ZDCF), with several changes that improve the performance of the DCF (Alexander 2013). The main advantages are the use of the z-transform and the equal population binning rather than equal lag $\Delta \tau$. These changes lead to a more robust method to compute the DCF under realistically unfavourable conditions (unevenly sampled and red noise dominated data; Alexander 1997, 2013). This method is limited by the number of points in the light curve. Due to the equal population binning, each bin has to contain at least 11 points, the minimum for a meaningful statistic interpretation. The binning algorithm leads to typical binning of our data of 20–30 d, except for the γ-ray light curves. Since these curves are almost evenly sampled, the width of the bins in these cases is the same as the sampling interval (7 d).

To test the periodicity hypothesis using the ZDCF method, we study the autocorrelation function. We follow the procedure described in McQuillan, Aigrain & Mazeh (2013) to estimate the period of the source. The first step is the identification of the peaks in the autocorrelation curve. To do so, since we are searching for long-term periods, we perform a smoothing of the curve to eliminate the variations and fluctuations introduced by short-term variability. This smoothing is implemented with the LOcally WEighted Scatter-plot Smoother method (Cleveland 1979), useful in detecting trends in noisy data. The basic approach of this method is to start with a local polynomial fit of order k (in this work, a linear regression is used) in the neighbourhood of each point, and use robust methods to obtain the final curve. A robust measurement of the period is obtained by calculating the median of the time lags that are approximately multiples of the same period.

We perform an estimation of the statistical significance of the resulting autocorrelation. High-significance correlation peaks can be produced by flare-like features in the light curve, well

described by red noise processes. To test whether the peaks are a true correlation or due to stochastic red noise processes, we need to quantify the significance of the peaks. For this purpose, we follow the procedure described in detail in Max-Moerbeck et al. (2014). Therefore, we simulate time series with the same statistical properties as our observations, i.e. with the same sampling as the light curves used in this work, and the same PSD and probability density function, and with no periodicity following the prescription from Emmanoulopoulos, McHardy & Papadakis (2013). This method has already been used in previous studies (e.g. Edelson et al. 1995; Chatterjee et al. 2008). Once a large number of random light curves has been simulated (10 000 in this work), we calculate the autocorrelation of each curve. Then, assuming a normal distribution of the autocorrelation coefficient in each bin, we estimate the statistical significance, i.e. the probability of obtaining an autocorrelation value due to stochastic red noise random processes. The statistical significance is given as multiples of the standard deviation, considering confidence levels (CL) from 1σ to 5σ, corresponding to probabilities of 68.27, 95.45, 99.73, 99.993666, and 99.99994267 per cent. Finally, the uncertainty of the resulting period is estimated using equation (3) in McQuillan et al. (2013).

Other effects should be taken into account as well when using the ZDCF, such as phase and amplitude variations, noise and systematic effects. These factors must be accounted when attempting to determine the true period of the signal (see McQuillan et al. 2013). The combination of all these effects can lead to features in the autocorrelation curve such as attenuation, alternating high and low peaks due to partial autocorrelation or long-term trends. In this case, the most important are attenuation, phase and amplitude variation, and linear trends and jumps in the light curves. Attenuation and amplitude variation introduce changes of the autocorrelation peak values in the ZDCF (observed for both sources, see the figures in Sections 4.1.1 and 4.2.1), while jumps in the light curve cause long-term trends on the ZDCF (see Section 4.1.1). These effects are present in the analysis; however, they can be distinguished from signatures of periodic variations in the light curves by looking at the ZDCF curve. If these effects are affecting the data series, fluctuations of the autocorrelation coefficient, changes in the amplitude of the peaks and trends in the ZDCF can be observed. A deeper discussion of all these biases is explained in detail in Alexander (2013).

3.2 Lomb–Scargle periodogram

The LS periodogram is one of the most used techniques in periodicity studies of unevenly sampled time series. This method is based on the discrete Fourier transform, but it differs from the classic periodogram so that the least-squares fit of the sine functions is minimized (Lomb 1976; Scargle 1982; VanderPlas 2018). This modification of the classic periodogram accounts for the problem of the irregularly sampled time series, avoiding interpolation, and the appearance of spurious peaks in the spectrum (Wang et al. 2014).

In order to compute and quantify the significance of the resulting peaks of the periodograms, we follow the procedure described by Vaughan (2005). Red noise processes can lead to spurious peaks and large fluctuations in the periodogram, specially at low frequencies (long time-scales). Assuming that the periodogram follows a power-law function model of the form $P(f) = Nf^{-\alpha}$, then the logarithm of the periodogram can be expressed as a linear function. Under these considerations, we can estimate the red noise continuum by fitting the logarithm of the periodogram with a linear function. With this

estimator, we can formulate the null hypothesis and calculate the probability that the data were produced by chance by a non-periodic signal. Adopting this method, the CLs in the periodogram also adopt a power-law shape. This power-law fit was also compared with the PSD estimation of the data to check their compatibility. All the fitted functions were found to be compatible with the derived PSDs of the light curves.

The uncertainty in the period determined with the LS is commonly given by the full width half-maximum (FWHM) of a Gaussian fit centred at the position of the maximum power of the corresponding peak (see Bhatta et al. 2016; Zhang et al. 2017a,b). This value only gives a rough estimation of the period uncertainty. For a more robust estimation, effects like spurious background peaks or aliases should be taken into account (VanderPlas 2018).

When using the LS periodogram, it is important to consider the caveats and limitations of the method. First, it is important to choose a proper frequency grid so as not to miss relevant information and to avoid a large computational burden. Also, one must take into account the possible appearance of spurious peaks due to harmonics of the true frequency and other kind of aliases that can introduce a sequence of false peaks, caused, for example, by annual observation patterns that can introduce a spike at a period of 1 yr (see VanderPlas 2018). All the effects commented in Section 3.1 also have their impact on the LS periodogram, leading to effects such as splitting or displacement of the true peaks or big bumps at a false frequency. Regarding the most important effects for our data, attenuation and amplitude variations cause the periodogram to produce two peaks on both sides on the correct period. Linear trends and jumps in the light curve introduce spurious peaks in the periodogram at large periods, which can lead to the wrong identification of the true period (McQuillan et al. 2013). In our analysis, we checked that the detected peaks do not correspond to harmonic peaks or sampling effects.

3.3 Weighted wavelet Z-transform

Alternatively to the traditional Fourier techniques for periodicity analysis, the wavelet transform is another widely used method due to its localization ability in both time and frequency domains (Torrence & Compo 1998), decomposing a time series into time–frequency space, finding the dominant modes of variability and their evolution with time. It is a powerful tool used for AGN variability studies (see Wang et al. 2014; An, Lu & Wang 2016; Bhatta et al. 2016).

An alternative and more suitable form of the wavelet technique for unevenly sampled data, the WWZ, is used in this work. It was developed to improve its performance under these conditions (Foster 1996), based on the Morlet wavelet (Grossmann, Kronland-Martinet & Morlet 1989; Han et al. 2012). This variation from the original method uses the z-transform and improves the performance of the wavelet transform under realistic conditions of unevenly sampled data series (Witt & Schumann 2005). Additionally, the PSD of the WWZ is calculated, giving the same information as the WWZ for a periodogram.

For an estimate of the significance, we follow a procedure similar to the one used for the LS periodogram (Section 3.2). We simulate 10 000 non-periodic light curves with the same sampling as our data. For each of these light curves, we compute the WWZ and the corresponding PSD. The significance is then calculated using the mean PSD of the simulated light curves as the non-periodic baseline following the method described in Vaughan (2005). Again, in the same way as in LS periodogram, the period uncertainty is given

by the FWHM of a Gaussian fit of the corresponding peak in the PSD. The same considerations we explained for the uncertainty estimation in the LS must be taken into account for the WWZ in order to make a more precise estimation of this value.

The main caveats and considerations when using the WWZ method are the choice of the wavelet function (width and shape of the function), the adequate time and frequency resolution, the choice of scales in order to have an optimal sampling, and the region in which edge effects become relevant due to the finite length of the time series, known as the cone of influence (COI), which can lead to the appearance of spurious peaks in the power spectrum of the WWZ (see Torrence & Compo 1998). An optimal sampling and scale were selected to perform this analysis, searching for a balance between the frequency resolution and computational time needed. Also, the effect of the COI was taken into account when calculating the WWZ, PSD, and significance of the data.

4 RESULTS

The periodicity analysis has been applied to the optical total flux in *R* and *V* bands, its polarization, and the γ-ray light curves, using the methods described in Section 3. The results for 3C 66A and B2 1633+38 are presented in Sections 4.1 and 4.2, respectively. The final results for each source are reported in Table 2.

4.1 3C 66A

4.1.1 Total optical magnitude

We analyse the *R* and *V* band light curves of 3C 66A with the three different methods presented in Section 3. We perform the analysis in magnitude scale instead of flux scale, since the latter is more biased towards large flares. Because of the better sampling, we focus on the results of the *R* band light curve. The *V* band light curve shows a largely uneven sampling and a poor time coverage in comparison with the *R* band ($\sim$50 observations per year and less than 700 total observations for the *V* band light curve, compared with more than 250 observations per year and more than 4000 observations in the case of the *R*-band light curve of this target). The results of the *V*-band light curve are presented in Fig. A1. The results of the *R*-band analysis are shown in Fig. 3.

The ZDCF in the *R* band for 3C 66A shows a clear sinusoidal shape as expected in case of a periodic behaviour, with a period of 2.98 ± 0.14 yr. The associated uncertainty is calculated using equation (3) in McQuillan et al. (2013). The significance of the peaks in the ZDCF varies between the 3σ and 5σ CL. Flare-like and short-term variability features are reflected in the curve as small fluctuations in the autocorrelation coefficient.

The resulting LS periodogram exhibits a prominent peak centred at a period value of 3.14 ± 0.24 yr, at a significance of $\sim$4σ. While the significance is lower than that obtained with the ZDCF method, the measured period is consistent. The periodogram also shows a secondary peak centred at a period of 2.28 yr. The existence of two peaks can be interpreted as a variation of the time-scale associated with two different activity states of the source. This can be tested by dividing the *R*-band light curve in two parts: the first one before MJD 55700, which corresponds to a possible high state of the source, with higher flux, in which a period of $\sim$3 yr is detected; and a second part from MJD 55700 onwards, which shows a possible low state of the source, and a period of $\sim$2.3 yr. The peak at a period of 2.28 yr is compatible with the results of the *V*-band light curve periodicity analysis shown in Fig. A1. This

Table 2. Results of the periodicity analysis of 3C 66A and B2 1633+38 for the *R* and *V* bands in both the total and polarized flux, and the high-energy γ-ray flux.

Source	Band	Method	Period (Yr)	Error (Yr)	Significance
3C 66A	*R* band	ZDCF	2.98	0.14	3σ–5σ
		LS	3.14	0.24	$\sim$$4\sigma$
			2.28	0.15	$>$$3\sigma$
		WWZ	2.92	0.79	$\sim$$4\sigma$
	V band	ZDCF	2.04	0.10	2σ–3σ
		LS	2.48	0.29	$\sim$$2\sigma$
		WWZ	2.28	0.47	$\sim$$3\sigma$
	Polarized *R* band	ZDCF	–	–	–
		LS	3.17	0.37	$<$$3\sigma$
		WWZ	3.07	0.4	$<$$3\sigma$
	γ-rays	ZDCF	–	–	–
		LS	–	–	–
		WWZ	–	–	–
B2 1633+38	*R* band	ZDCF	1.80	0.04	2σ–5σ
		LS	1.80	0.10	$>$$4\sigma$
		WWZ	1.89	0.48	$\sim$$4\sigma$
	V band	ZDCF	1.91	0.05	2σ–5σ
		LS	1.85	0.17	$>$$4\sigma$
		WWZ	1.93	0.40	$>$$5\sigma$
	Polarized *R* band	ZDCF	1.79	0.06	2σ–$>$$4\sigma$
		LS	1.81	0.12	$>$$4\sigma$
		WWZ	1.92	0.57	$>$$4\sigma$
	γ-rays	ZDCF	1.59	0.07	3σ–4σ
		LS	1.77	0.12	$\sim$$2\sigma$
		WWZ	1.75	0.48	$\sim$$2\sigma$

latter value is also consistent with the possible long-term quasi-periodicities found by Belokon & Babadzhanyants (2003) and Kaur et al. (2017). Furthermore, a peak above the 4σ CL is found at a period of $\sim$180 d. This peak is compatible with the period detected by Fan et al. (2018) with a value of 156 ± 17 d in the *R* band, and 156 ± 15 d in the *I* band.

The colour-scaled histogram of the WWZ shows a periodic feature, also reflected on the PSD, centred at 2.92 ± 0.79 yr at $\sim$$4\sigma$ CL. This result is consistent with those derived from the ZDCF and the LS methods. Non-significant peaks due to flare-like short-term variability can be identified in the PSD curve, and can also be seen in the colour-scaled power representation of the WWZ at lower values of the period. At long periods, the effect of the red noise becomes more important, introducing a bump above $\sim$6 yr. The *V*-band WWZ presents only the secondary peak, centred at 2.27 ± 0.47 yr at a CL of $\sim$$3\sigma$. Since almost all of the *V*-band data were obtained during the relatively fainter epoch, all the previous results are consistent.

4.1.2 Polarized optical magnitude

The periodicity analysis was performed on the polarized data provided by the Steward observatory, the polarimetric observations of the St. Petesburg University made in St. Petersburg and the CrAO. The results are presented in Fig. 4. 3C 66A shows no hints for periodic behaviour with any of the used techniques in this work. The ZDCF has no periodic structure, with no significant peaks that can be associated with a periodic emission. A strong fluctuation at a time delay of $\sim$2000 d appears, but since there is no periodic structure in the curve and no other method agrees with this peak, it is likely due to a non-periodic emission process. Also, at such high time delays, only a small part of the light curve is being compared,

so it is more probable to find randomly high autocorrelation values. The LS periodogram and the wavelet analysis show no significant long-term variability peaks reaching a significance of 3σ around the period seen for the total magnitude. However, a shorter period peak appears in the LS with a period of 178 d at a CL of $\sim$$4\sigma$. This peak is consistent with the one seen in the total flux periodogram with a period of 180 d.

This absence of long-term periodicity in the optical polarized light curve of 3C 66A is in agreement with the lack of correlation observed between the optical magnitude and the polarization degree. This result is shown in Fig. 5. There is no correlated behaviour between the magnitude and the polarization of this source. We performed an estimation of the Spearman's rank correlation coefficient (ρ) to quantify the degree of (non-) correlation observed in 3C 66A, obtaining a value of $\rho = 0.17$, $p = 0.0017$ between the polarization degree and the *R*-band magnitude, where p is the probability for null hypothesis.

4.1.3 γ-ray flux

We have also searched for possible periodicity of this source in the HE γ-ray regime with the light curve extracted from the *Fermi–LAT* data. All three methods agree that there is no indication of long-term periodicity in the γ-ray emission of 3C 66A. There is no periodic structure or fluctuation in the ZDCF and no significant peaks in the periodogram or the wavelet transform (Fig. 6).

4.2 B2 1633+38

4.2.1 Total optical magnitude

In the case of B2 1633+38, we are presenting both *R* and *V* bands, since both have a good temporal coverage and sampling,
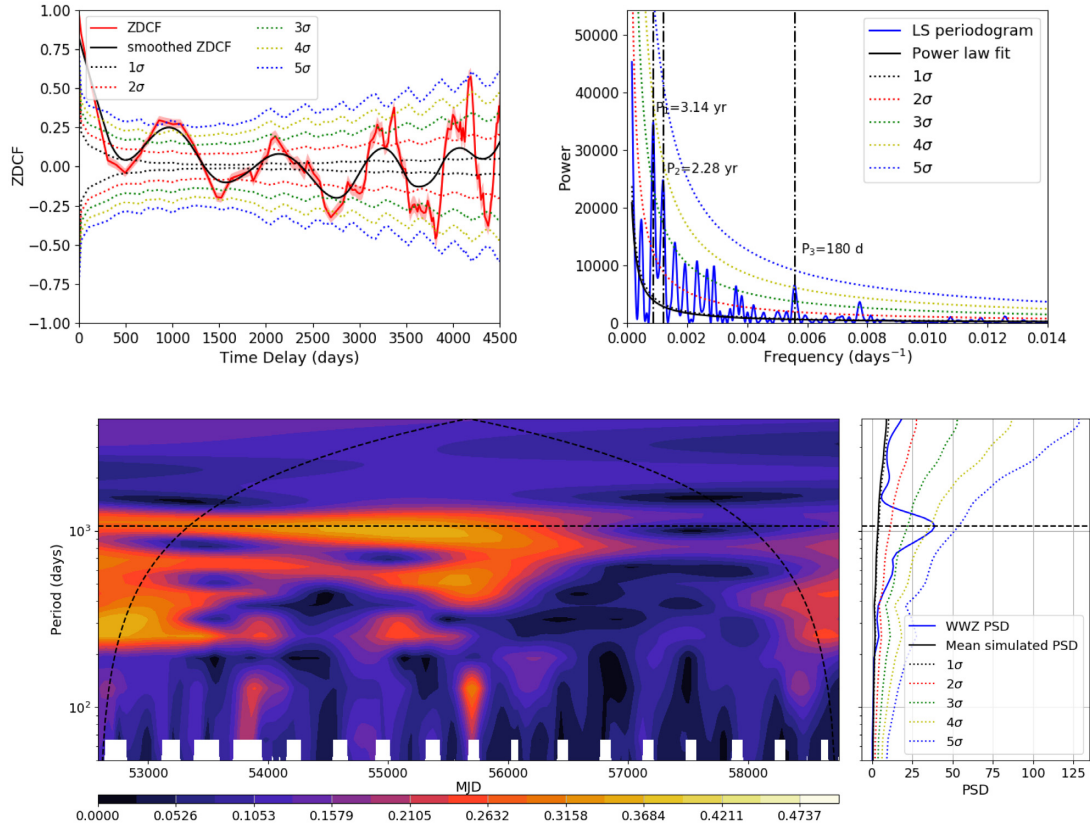
Figure 3. Periodicity analysis of the *R*-band data of 3C 66A. *Top left*: ZDCF method. The autocorrelation curve is given in red and the smoothed curve in black. *Top right*: Lomb–Scargle periodogram. The periodogram is given in blue and the power-law fit in black. *Bottom*: WWZ method. The left-hand panel shows the 2D power spectrum as a function of period and time. The black-dashed curve represents the COI. The right-hand panel shows the PSD in blue and the mean simulated PSD in black. The coloured-dotted lines represent the different significance levels. The black horizontal dashed line marks the peak of the PSD.

as shown in Fig. 2. The results of all three methods are shown in Fig. 7. The ZDCF presents a sinusoidal shape characteristic of a periodic component to its optical emission. The measured period with this method has a value of 1.91 ± 0.05 yr for the *V* band and 1.80 ± 0.04 yr for the *R* band. The maxima and minima of the curve reach significances between 2σ and 5σ. Flare-like features on the light curve can be seen in the ZDCF as fluctuations in the autocorrelation coefficient, as is seen for 3C 66A.

The LS periodograms peak at a period of 1.85 ± 0.17 yr in the *V* band and at 1.80 ± 0.10 yr in the *R* band. These values are compatible with those calculated with the autocorrelation method within their uncertainties. The significance of the peaks reaches values slightly higher than 4σ in both cases. Also, a secondary peak (above 3σ CL) with a period of 117 d is found in the *V*-band periodogram.

Regarding the WWZ for this source, there is also an agreement with the two other methods. The measured values of the period with the wavelet transform are 1.93 ± 0.40 yr in the *V* band, with a significance above 5σ, and 1.89 ± 0.48 yr in the *R* band, at the 4σ CL. The results of all three methods for the analysis of B2 1633+38 can be seen in Table 2 for both filters, with their corresponding uncertainties and significance levels.

4.2.2 Polarized optical magnitude

Contrary to what has been seen on 3C 66A, this source does exhibit a possible periodic variability also in the polarized magnitude light curve. The results of the analysis are shown in Fig. 8. The ZDCF curve shows the same behaviour as for the total flux, having a sinusoidal shape with alternating maxima and minima at CL between $\sim 2\sigma$ and almost 5σ. The variability time-scale measured with this method is 1.79 ± 0.06 yr. The LS periodogram reveals a prominent peak at a period value of 1.81 ± 0.12 yr with a significance of $\sim 4\sigma$, compatible with both the ZDCF and the total flux case. Finally, the WWZ and its corresponding PSD estimate a period of 1.92 ± 0.57 yr above the 4σ CL in agreement with the two other methods. This result is expected on the basis of the strong correlation between continuum flux and polarization degree found by Raiteri et al. (2012). This correlated behaviour between the polarization and the flux can be seen in Fig. 9. The polarization degree shows a positive correlation with the total optical magnitude for B2 1633+38 with a Spearman's correlation coefficient of $\rho = 0.46$, $p < 0.001$. In addition, hints of periods on the order of ~ 100 d at CL of $\sim 3\sigma$ are found in the LS periodogram for both total and polarized optical flux, and also a peak with a period of ~ 170 d at CL of $\sim 4\sigma$ in the polarized magnitude periodogram.
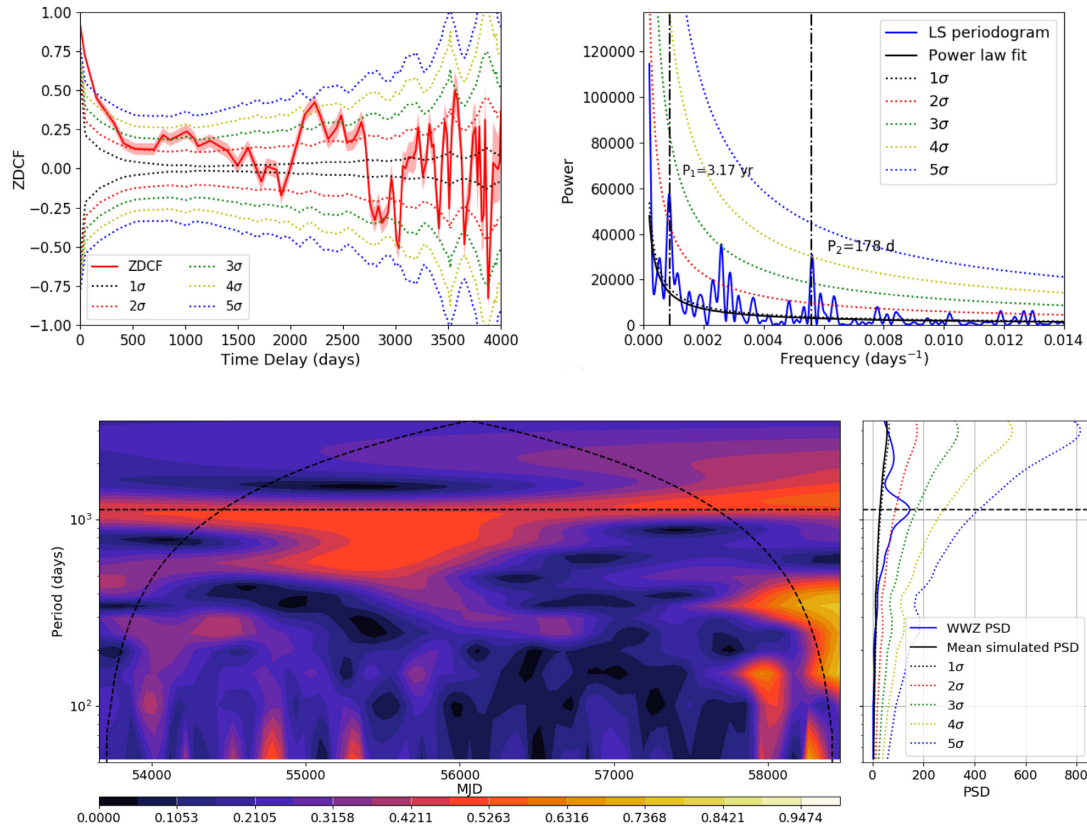
Figure 4. Periodicity analysis of the polarized *R*-band data of 3C 66A. Same description as Fig. 3.
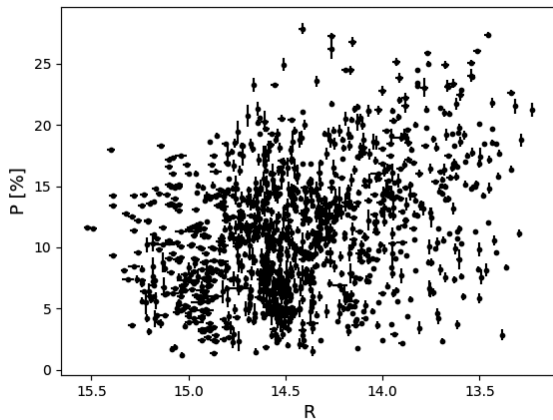

Figure 5. The observed polarization degree against the *R*-band total magnitude for 3C 66A. These two quantities have a Spearman's correlation coefficient of $\rho = 0.17$.

4.2.3 *γ-ray flux*

The γ-ray variability analysis, as it happened with the optical total and polarized magnitude light curve analysis, shows a hint of periodic variability on the time-scale of ~ 2 yr. The results of the γ-ray band analysis are presented in Fig. 10. The ZDCF shows a series of maxima and minima with a periodicity of 1.59 ± 0.07 yr and significances of ~ 3–4σ with a periodic structure starting at a time lag of 1500 d. Up to that delay, the ZDCF shows no prominent peak, with an autocorrelation coefficient close to zero. This can

be explained by observing the corresponding light curve. During the first 2000 d there were three major outbursts, and afterwards the γ-ray flux seems to be in a quiescent state that finishes at MJD 58000, when another outburst commences. This quiescent state may be the reason why an autocorrelation value close to zero at delays shorter than 1500 d is observed. It suggests that there is no real periodic behaviour, but a series of unrelated and equidistant flares. However, we cannot exclude the possibility that the limited sensitivity of *Fermi–LAT* prevented us from detecting lower amplitude periodic flares during the quiescent period. In this case, we are only smoothing the part of the ZDCF with the prominent peaks to estimate time lags and derive the period value. A peak in both the LS periodogram and the PSD of the wavelet transform with approximately the same CL and consistent period values appears to support a possible periodic variation (1.77 ± 0.12 yr with the periodogram and 1.75 ± 0.48 yr with the wavelet transform). These results are not significant enough to claim for a solid periodic detection, however, Raiteri et al. (2012) found a strong correlation between optical and γ-ray flares. Despite that, flux ratios change with time and there is a general trend for the optical variations to follow those observed in the γ-rays by few days. This fact gives marginal support to our finding of quasi-periodic variations at HEs. Two more peaks appear at higher periods (~ 3 yr and ~ 6 yr). The 3 yr peak seems incompatible with the results of the ZDCF and the optical curves, and also inconsistent with time lags between flares in the *Fermi–LAT* light curve, so it is not considered as possible period. The 6 yr peak is identified as red noise. A peak with a period value of ~ 264 d is also identified in the LS periodogram at a CL of 3σ that could be indicative of a type of variability in shorter time-scales.
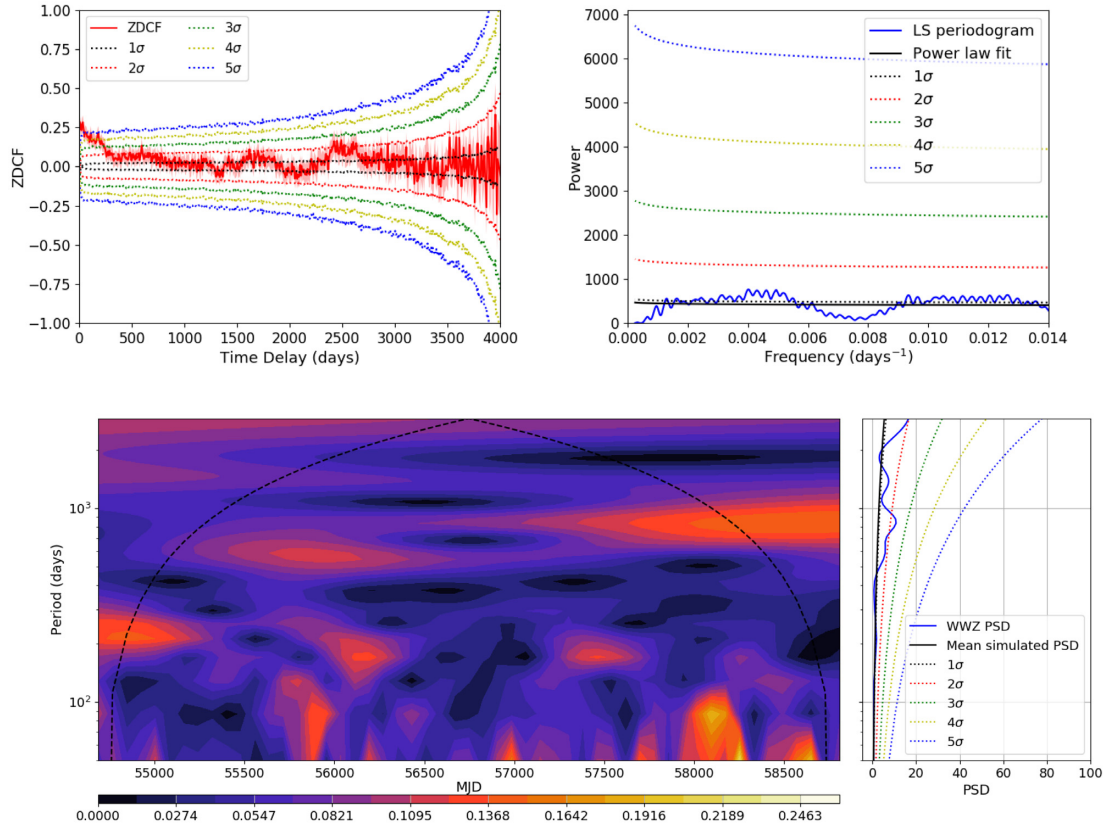
Figure 6. Periodicity analysis of the γ-ray flux for 3C 66A. Same description as Fig. 3.

5 DISCUSSION

After the analysis of both the total and polarized optical magnitude light curves, we can highlight the different behaviour observed in these two sources. While 3C 66A shows a clear period only in the total optical light curve, B2 1633+38 behaves periodically for both total and polarized light. This difference can also be appreciated in the HE γ-ray regime. 3C 66A shows no long-term variability, with variations only at short time-scales. Moreover, the HE emission of B2 1633+38 exhibits a hint of a periodic flux variability. However, the confirmation of Quasi-periodic oscillations (QPOs) in γ-ray with *Fermi–LAT* data, previously claimed by other authors, has been questioned by Covino, Sandrinelli & Treves (2019).

Year-like time-scale quasi-periodicities shown in blazars have been interpreted within various scenarios (e.g. Ackermann et al. 2015b; Sandrinelli et al. 2016), and can be grouped into two general cases:

(i) The existence of a SBBH, as proposed for OJ 287 (Sillanpaa et al. 1988; Lehto & Valtonen 1996; Villata & Raiteri 1999); or PG 1302-102 (Graham et al. 2015). The presence of a second perturbing black hole could either modulate the accretion rate or produce a precession in the jet(s). Models based on an SBBH system have been proposed (Caproni et al. 2017; Cavaliere, Tavani & Vittorini 2017; Sobacchi, Sormani & Stamerra 2017) and applied to the case of PG 1553+113 (Ackermann et al. 2015b). Sobacchi et al. (2017) proposed a simple spine-sheath precessing jet model, which is able to reproduce the recurrence observed in the optical and γ-ray light curves and the SED of the source from the optical to the X-ray bands. Hudec & Basta (2006) favour this model for 3C 66A and include the source as a candidate to harbor an SBBH.

However, the hypothesis of an SBBH to explain all observed quasi-periodic behaviour in blazars can be ruled out according to the recent work by Sandrinelli et al. (2018) who compared the prevalence of quasi-periodic behaviour between bright γ-ray blazars and quasars. Sandrinelli et al. (2018) found that the local density of quasi-periodic blazars is much larger than that of quasars. On the other hand, Sesana et al. (2018) found that if all quasi-periodic quasars involved an SBBH system, then the expected gravitational wave background at frequencies corresponding to year time-scales would be in conflict with that measured with pulsar timing arrays (Foster & Backer 1990). Holgado et al. (2018) similarly concluded that binarity cannot uniquely explain quasi-periodicity in the *Fermi* blazar population on time-scales of a few years.

(ii) Variations in the relativistic jet emission mechanism, either due to geometrical effects such as helical jets or helical structures in the jet (Camenzind & Krockenberger 1992; Rieger 2004; Mohan & Mangalam 2015). The emitting flow moving around an helical path could produce relatively long-term quasi-periodic changes in Doppler boosted flux (Villata & Raiteri 1999; Ostorero, Villata & Raiteri 2004; Raiteri et al. 2010). In this case, the variation is produced by geometrical effects due to changes in the viewing angle or the observation of different emitting regions of the jet at different times. In a recent work, Casadio et al. (2019) found evidence for the presence of large-scale helical magnetic fields from high-resolution mm-VLBI observations of CTA 102. Raiteri et al. (2017) could explain a large flare in CTA 102 occurring at the end of 2016 as variations in the orientation of the viewing angle of the jet emitting regions and, hence, their relative Doppler factors. They propose that the orientation of different jet regions may change due to magnetohydrodynamic (MHD) instabilities (Mignone et al.
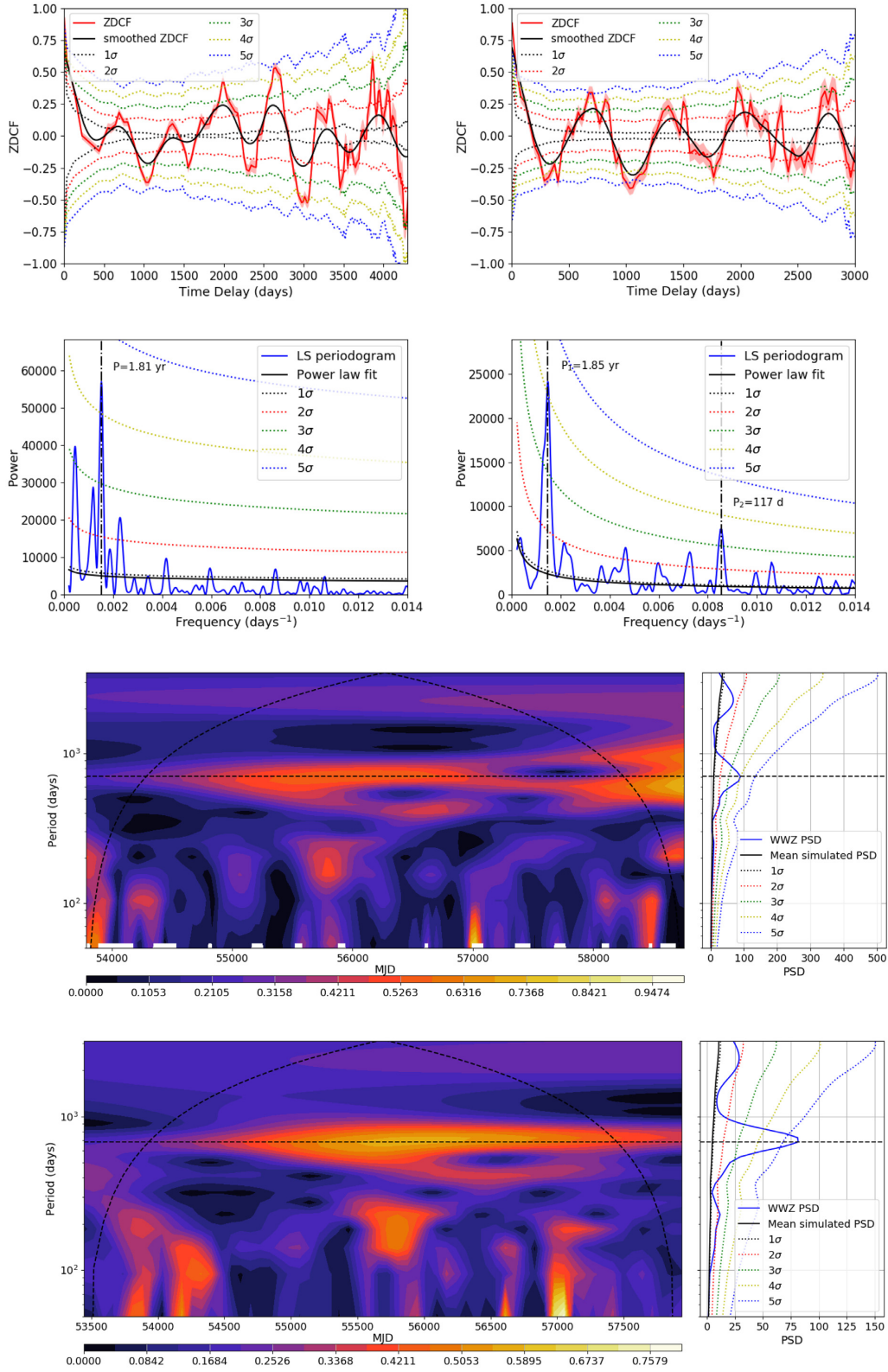
Figure 7. Periodicity analysis of B2 1633+38. *First row*: ZDCF method in *R* (left) and *V* (right) bands. The autocorrelation curve is given in red and the smoothed curve in black. *Second row*: Lomb–Scargle periodogram in *R*(left) and *V* (right) bands. The periodogram is given in blue and the power-law fit in black. *Third row*: WWZ diagram in the *R* band. *Fourth row*: WWZ diagram in the *V* band. The left-hand panels show the 2D power spectrum as a function of period and time. The black-dashed curves represent the COI. The right-hand panels show the PSD in blue and the mean simulated PSD in black. The coloured-dotted lines represent the different significance levels. The black horizontal dashed lines mark the peak of the PSD.
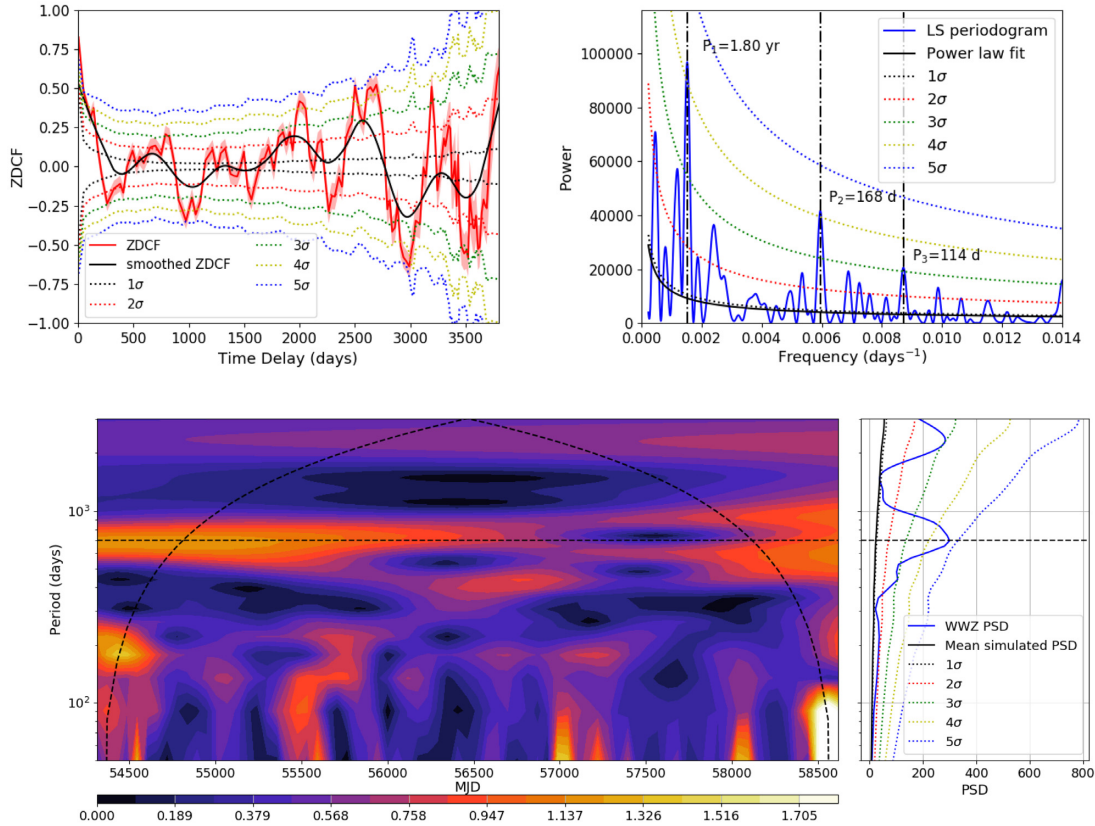
Figure 8. Periodicity analysis of the polarized *R*-band data of B2 1633+38. Same description as Fig. 3.
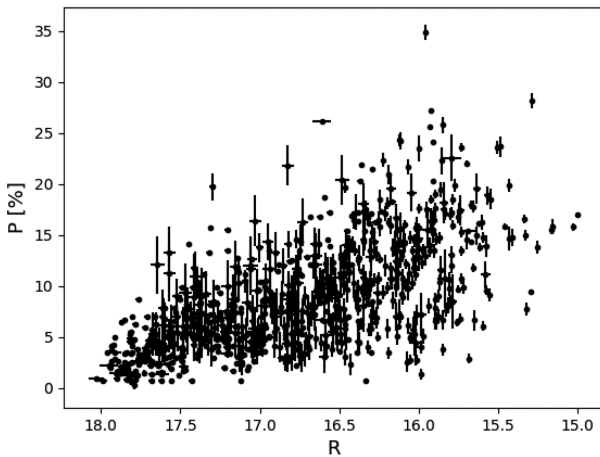
Figure 9. The observed polarization degree against the *R*-band total magnitude for B2 1633+38. These two quantities have a Spearman's correlation coefficient of $\rho = 0.46$.

2010) or rotation of a twisted jet. Indeed, jets show large-scale inhomogeneities that can be attributed to different mechanisms: re-confinements and relativistic shocks (Marscher & Gear 1985), Kelvin–Helmholtz instabilities, helical patterns, or turbulent cells (Marscher 2014). Alternatively, variations in the energy outflow of the jet could be induced by instabilities in the accretion flow (Tchekhovskoy et al. 2011; Godfrey et al. 2012). The innermost part of accretion discs around supermassive black holes is pulsationally unstable. MHD simulations of magnetically choked accretion flows

have shown that oscillations with a period of tens of days can be produced in an accretion disc around a spinning black hole of $M_{\mathrm{BH}} \simeq 10^9 \, \mathrm{M_\odot}$ (McKinney, Tchekhovskoy & Bland ford 2012). This period is still relatively short compared to those found in this work.

There may be different mechanisms responsible for the two cases that we have analysed. 3C 66A is a BL Lac object, which is supposed to contain a radiatively inefficient accretion disc (Fragile & Meier 2009). A plausible mechanism could be disc instabilities transmitted to the jet (Godfrey et al. 2012), but not affecting the disc emission. In this scenario, there is no clear reason to expect a correlation between the total and polarized flux, since these instabilities should propagate through the jet without affecting any structure such as magnetic fields that can affect the polarization of the emitted flux. However, this model may be disfavoured by the time-scales involved in this scenario, on the order of 10^3 yr for black hole masses of $\sim 10^8 \, \mathrm{M_\odot}$ (Godfrey et al. 2012). On the other hand, the fact that we find quasi-periodic behaviour not only in integrated light, but also its linear polarization and a possible hint at HEs in B2 1633+38 indicates that the responsible mechanism must be persistent in time. B2 1633+38 is a high-luminosity FSRQ blazar, that may develop a powerful jet with stable structures such as helical structures, reconfinements, or shock fronts, in a precessing or bent structure. The idea of an helical-like magnetic field is favoured by Hagen-Thorn et al. (2019), based on the different directions of the polarization vector in different epochs. Moreover, a shock wave propagating along a helical path in the blazar's jet was proposed to explain the multifrequency behaviour of an outburst in 2011 of the blazar S5 0716+71 (Larionov et al. 2013). The strong correlation
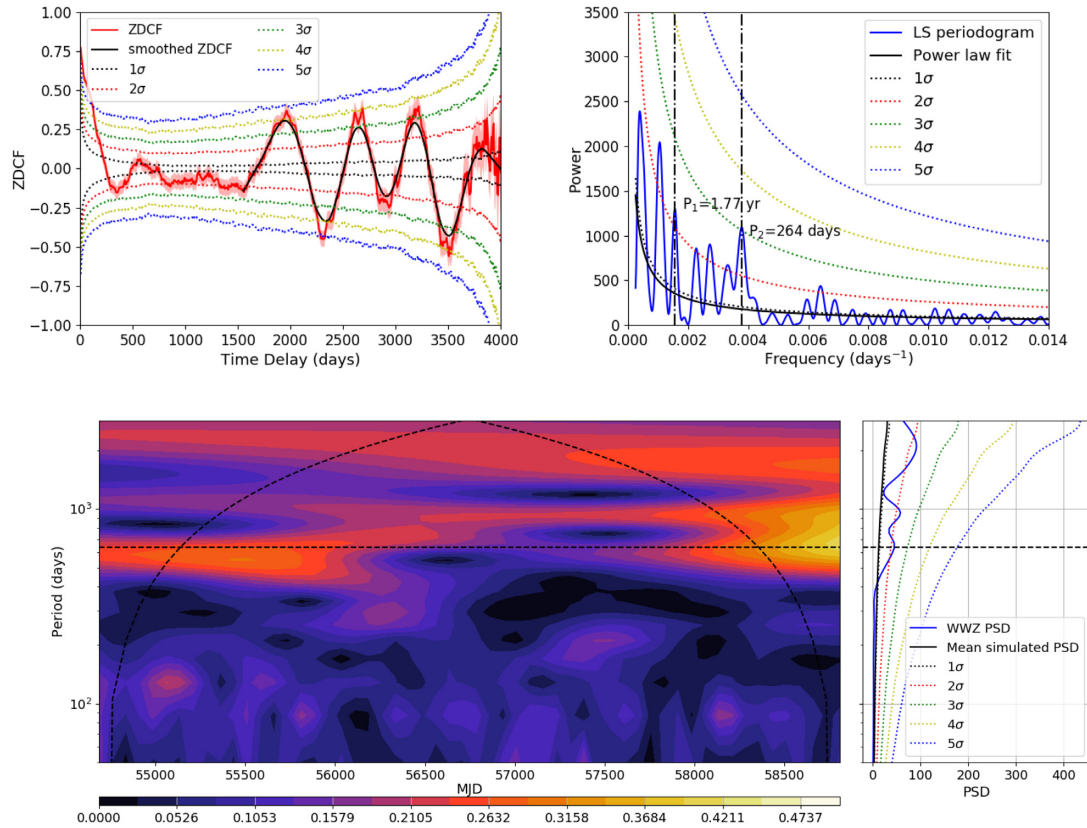
Figure 10. Periodicity analysis of the γ-ray flux for B2 1633+38. *Top left*: ZDCF method. The autocorrelation curve is given in red and the smoothed curve in black. *Top right*: Lomb–Scargle periodogram. The periodogram is given in blue and the power-law fit in black. *Bottom*: WWZ diagram. The left-hand panel shows the 2D power spectrum as a function of period and time. The black-dashed curve represents the COI. The right-hand panel shows the PSD in blue and the mean simulated PSD in black. The coloured-dotted lines represent the different significance levels. The black horizontal dashed line marks the peak of the PSD.

between continuum flux and polarization degree of B2 1633+38 is consistent with the result found by Raiteri et al. (2012) using a much shorter time window. Such behaviour was explained in terms of an inhomogeneous jet in which variability is caused by changes of the emitting region viewing angle, $\theta = 2.6°$–$5.3°$, coupled with a high Lorentz factor $\Gamma = 31.1$ (see also Raiteri et al. 2013). Different jet models, helical magnetic fields by Lyutikov, Pariev & Gabuzda (2005) or transverse shock waves (Hughes, Aller & Aller 1985), predict a maximum value for the polarization degree at the viewing angle, $\theta_{max} \sim 1/\Gamma$. For viewing angles smaller than θ_{max}, the polarization decreases, whereas the flux increases when the angle gets closer to zero, due to Doppler boosting. The opposite happens for viewing angles larger than θ_{max}, then a positive correlation is observed between the flux and the polarization degree, as proposed for B2 1633+38. In the case of 3C 66A, the same model could be applied considering a smaller Lorentz factor, $\Gamma = 16.1$ (Celotti & Ghisellini 2008; Jorstad et al. 2017) and a similar viewing angle, $\theta = 1.5°$–$4.5°$ (fig. 17 in Raiteri et al. 2013). In this case, the viewing angle is close to θ_{max}, and no strong correlation is expected between total and polarized optical fluxes. Note that determination of Lorentz factor and inclination angles depends largely on the used method: rapid variability observed at HEs and modelling of SEDs usually predict very high values for Γ (50–100), whereas high-resolution radio observations (VLBA) imply much lower values for Γ (the so-called Doppler crisis, see Tavecchio 2006; Piner & Edwards 2018). Furthermore, the determination of Γ based on VLBA observations depends on the knotty structure observed in the relativistic jet (e.g.

for 3C 66A, Jorstad et al. 2017 found $\Gamma \sim 30$ and $\Gamma \sim 13$ for knots B1 and B2, respectively).

On the other hand, detection of quasi-periodicity on different time-scales in the same object may suggest the presence of several inhomogeneities in the jet structure. This behaviour is more difficult to explain with an SBBH model scenario in which a single quasi-periodicity time-scale is expected. Moreover, this model predicts quasi-periodicities in time-scales >10 yr (e.g. Romero et al. 2000). Shorter time-scales explained with an SBBH model would imply very close binary systems. The detection of these systems is very improbable due to their very short lifetime (Rieger 2019).

6 CONCLUSIONS

We studied the total and polarized optical flux in *V* and *R* bands, along with the γ-ray emission of the BL Lac object 3C 66A and the FSRQ B2 1633+38, searching for quasi-periodic variability. The optical and polarized light curves extend more than 14 yr for 3C 66A and more than 12 yr for B2 1633+38, while the γ-ray light curves span nearly 11 yr. For this purpose, we used the different methods to perform the variability analysis such as the ZDCF, the LS periodogram, and the WWZ.

Evidence of quasi-periodic variability was found in the optical light curves of 3C 66A with a period of $\sim$3 yr at a CL of between 2σ and 5σ depending on the analysis method. Also, a possible secondary period of $\sim$2.3 yr was found in the *R* band by dividing the light curve into a high state part compatible with the 3 yr

period, and a low state part that shows this shorter period value, which is compatible with the results presented by Belokon & Babadzhanyants ([2003](#)) and Kaur et al. ([2017](#)). In addition, we identified a period of ∼180 d, previously detected by Fan et al. ([2018](#)). No periodic behaviour was seen neither in the polarized or γ-ray light curves.

On the other hand, pieces of evidence of quasi-periodicity were detected in both the optical total and polarized flux light curves of B2 1633+38, with an approximate period of ∼1.9 yr at a CL of between 2σ and 5σ depending on the variability analysis method used. This appears to be the first report of quasi-periodic variability in optical polarized emission from a blazar and is a consequence of the periodicity detected in the total flux combined with the correlation between flux and the polarization degree pointed out by Raiteri et al. ([2012](#)). A hint of periodicity was also detected in the γ-ray light curve of this source. However, the emission is dominated by flares only during a part of the γ-ray light curve, combined with a long quiescent state. Thus, we cannot confirm that the recurrence of these flares is periodic, or produced by chance.

Different jet emission mechanisms were proposed to account for the results. While periodicity in 3C 66A could be supported by SBBH models due to the source being radiatively inefficient (Fragile & Meier [2009](#)) and a being classified as a SBBH candidate (Hudec & Basta [2006](#)), the periodicity in B2 1633+38 may be explained by geometrical effects in the jet such as helical structures or shock fronts (Marscher & Gear [1985](#); Marscher [2014](#)). The same scenario could also be valid in the case of 3C 66A. Based only on the results for two blazars, we obviously cannot generalize the assignment of different mechanisms causing periodic variability behaviour to BL Lac objects and FSRQs. Future studies of larger samples of blazars will need to be made to clarify the nature of quasi-periodic variability in blazars.

REFERENCES

Abdo A. A. et al., 2011, ApJ, 726, 43
Acciari V. A. et al., 2009, ApJ, 693, L104
Ackermann M. et al., 2015a, ApJ, 810, 14
Ackermann M. et al., 2015b, ApJ, 813, L41
Ackermann M. et al., 2016, ApJS, 222, 5
Aleksić J. et al., 2011, ApJ, 726, 58
Alexander T., 1997, in Maoz D., Sternberg A., Leibowitz E. M., eds, Astronomical Time Series. Kluwer, Dordrecht, p. 163
Alexander T., 2013, preprint (arXiv:1302.1508)
An T., Lu X.-L., Wang J.-Y., 2016, A&A, 585, A89
Atwood W. B. et al., 2009, ApJ, 697, 1071
Barbieri C., Romano G., di Serego S., Zambon M., 1977, A&A, 59, 419
Belokon E. T., Babadzhanyants M. K., 2003, ASP Conf. Ser. Vol. 299, High Energy Blazar Astronomy. San Francisco, Astron. Soc. Pac., p. 205
Bhatta G. et al., 2016, ApJ, 832, 47
Bonning E. W. et al., 2009, ApJ, 697, L81
Böttcher M., 2019, Galaxies, 7, 20
Böttcher M. et al., 2005, ApJ, 631, 169
Böttcher M. et al., 2009, ApJ, 694, 174
Camenzind M., Krockenberger M., 1992, A&A, 255, 59
Caproni A., Abraham Z., Motter J. C., Monteiro H., 2017, ApJ, 851, L39
Carnerero M. I. et al., 2015, MNRAS, 450, 2677
Casadio C. et al., 2019, A&A, 622, A158
Cavaliere A., Tavani M., Vittorini V., 2017, ApJ, 836, 220
Celotti A., Ghisellini G., 2008, MNRAS, 385, 283
Chatterjee R. et al., 2008, ApJ, 689, 79
Chatterjee R. et al., 2012, ApJ, 749, 191
Cleveland W. S., 1979, J. Am. Stat. Assoc., 74, 829
Covino S., Sandrinelli A., Treves A., 2019, MNRAS, 482, 1270
de Diego J. A., Kidger M. R., Gonzalez-Perez J. N., Lehto H. J., 1997, A&A, 318, 331
Drake A. J. et al., 2009, ApJ, 696, 870
Edelson R. et al., 1995, ApJ, 438, 120

Edelson R. A., Krolik J. H., 1989, in Osterbrock D. E., Miller J. S., eds, Proc. IAU Symp. 134, Active Galactic Nuclei. Kluwer, Dordrecht, p. 96

Emmanoulopoulos D., McHardy I. M., Papadakis I. E., 2013, MNRAS, 433, 907

Fan J. H. et al., 2006, Chin. J. Astron. Astrophys. Suppl., 6, 333

Fan J. H. et al., 2018, AJ, 155, 90

Finke J. D., 2013, ApJ, 763, 134

Finke J. D., Shields J. C., Böttcher M., Basu S., 2008, A&A, 477, 513

Foster G., 1996, AJ, 112, 1709

Foster R. S., Backer D. C., 1990, ApJ, 361, 300

Fragile P. C., Meier D. L., 2009, ApJ, 693, 771

Furniss A., Fumagalli M., Danforth C., Williams D. A., Prochaska J. X., 2013, ApJ, 766, 35

Ghosh K. K., Soundararajaperumal S., 1995, ApJS, 100, 37

Godfrey L. E. H. et al., 2012, ApJ, 758, L27

Graham M. J. et al., 2015, Nature, 518, 74

Grossmann A., Kronland-Martinet R., Morlet J., 1989, in Combes J.-M., Grossmann A., Tchamitchian P., eds, Proceedings of the International Conference, Wavelets. Time–frequency Methods and Phase Space. Springer-Verlag, Berlin, p. 2

Gupta A., 2018, Galaxies, 6, 1

Hagen-Thorn V. A. et al., 2019, Astron. Rep., 63, 378

Han X., Wang J., Lin J., An T., 2012, 2012 8th International Conference on Wireless Communications, Networking and Mobile Computing. IEEE, Piscataway, NJ, p. 1

Holgado A. M., Sesana A., Sandrinelli A., Covino S., Treves A., Liu X., Ricker P., 2018, MNRAS, 481, L74

Hovatta T., Tornikoski M., Lainela M., Lehto H. J., Valtaoja E., Torniainen I., Aller M. F., Aller H. D., 2007, A&A, 469, 899

Hudec R., Basta M., 2006, Chin. J. Astron. Astrophys. Suppl., 6, 253

Hughes P. A., Aller H. D., Aller M. F., 1985, ApJ, 298, 301

Jorstad S. G. et al., 2017, ApJ, 846, 98

Kaur N., Sameer, Baliyan K. S., Ganesh S., 2017, MNRAS, 469, 2305

Lainela M. et al., 1999, ApJ, 521, 561

Larionov V. M. et al., 2013, ApJ, 768, 40

Lehto H. J., Valtonen M. J., 1996, ApJ, 460, 207

Li W., Filippenko A. V., Chornock R., Jha S., 2003, PASP, 115, 844

Liao N. H., Bai J. M., Liu H. T., Weng S. S., Chen L., Li F., 2014, ApJ, 783, 83

Liu X. et al., 2017, MNRAS, 469, 2457

Liu Y., Jiang D. R., Shen Z.-Q., Karouzos M., 2010, A&A, 522, A5

Lomb N. R., 1976, Ap&SS, 39, 447

Lyutikov M., Pariev V. I., Gabuzda D. C., 2005, MNRAS, 360, 869

Marscher A. P., 2014, ApJ, 780, 87

Marscher A. P., Gear W. K., 1985, ApJ, 298, 114

Max-Moerbeck W., Richards J. L., Hovatta T., Pavlidou V., Pearson T. J., Readhead A. C. S., 2014, MNRAS, 445, 437

McKinney J. C., Tchekhovskoy A., Bland ford R. D., 2012, MNRAS, 423, 3083

McQuillan A., Aigrain S., Mazeh T., 2013, MNRAS, 432, 1203

Mignone A., Rossi P., Bodo G., Ferrari A., Massaglia S., 2010, MNRAS, 402, 7

Miller J. S., French H. B., Hawley S. A., 1978, in Wolfe A. M., ed., Pittsburgh Conference on BL Lac Objects. University of Pittsburgh, Pittsburgh, PA, p. 176

Mohan P., Mangalam A., 2015, ApJ, 805, 91

Ostorero L., Villata M., Raiteri C. M., 2004, A&A, 419, 913

Paiano S., Landoni M., Falomo R., Treves A., Scarpa R., Righi C., 2017, ApJ, 837, 144

Pâris I. et al., 2017, A&A, 597, A79

Piner B. G., Edwards P. G., 2018, The Fourteenth Marcel Grossmann Meeting On Recent Developments in Theoretical and Experimental General Relativity, Astrophysics, and Relativistic Field Theories. World Scientific Press, Singapore, p. 3074

Raiteri C. M. et al., 2010, A&A, 524, A43

Raiteri C. M. et al., 2012, A&A, 545, A48

Raiteri C. M. et al., 2013, MNRAS, 436, 1530

Raiteri C. M. et al., 2017, Nature, 552, 374

Rajput B., Stalin C. S., Sahayanathan S., Rakshit S., Mandal A. K., 2019, MNRAS, 486, 1781

Rieger F. M., 2004, ApJ, 615, L5

Rieger F., 2019, Galaxies, 7, 28

Romero G. E., Chajet L., Abraham Z., Fan J. H., 2000, A&A, 360, 57

Romero G. E., Boettcher M., Markoff S., Tavecchio F., 2017, Space Sci. Rev., 207, 5

Sandrinelli A., Covino S., Dotti M., Treves A., 2016, AJ, 151, 54

Sandrinelli A., Covino S., Treves A., Holgado A. M., Sesana A., Lindfors E., Ramazani V. F., 2018, A&A, 615, A118

Scargle J. D., 1982, ApJ, 263, 835

Sesana A., Haiman Z., Kocsis B., Kelley L. Z., 2018, ApJ, 856, 42

Sillanpaa A., Haarala S., Valtonen M. J., Sundelius B., Byrd G. G., 1988, ApJ, 325, 628

Smith P. S., Montiel E., Rightley S., Turner J., Schmidt G. D., Jannuzi B. T., 2009, preprint (arXiv:0912.3621)

Sobacchi E., Sormani M. C., Stamerra A., 2017, MNRAS, 465, 161

Strassmeier K. G. et al., 2004, Astron. Nachr., 325, 527

Tavecchio F., 2006, The Tenth Marcel Grossmann Meeting. Proceedings of the MG10 Meeting held at Brazilian Center for Research in Physics (CBPF), Rio de Janeiro, Brazil, 20-26 July 2003. World Scientific Press, Singapore, p. 512

Tchekhovskoy A., Narayan R., McKinney J. C., 2011, MNRAS, 418, L79

The Fermi-LAT collaboration, 2019, preprint (arXiv:1902.10045)

Torrence C., Compo G. P., 1998, Bull. Am. Meteorol. Soc., 79, 61

Torres-Zafra J., Cellone S. A., Buzzoni A., Andruchow I., Portilla J. G., 2018, MNRAS, 474, 3162

Urry C. M., Padovani P., 1995, PASP, 107, 803

VanderPlas J. T., 2018, ApJS, 236, 16

Vaughan S., 2005, A&A, 431, 391

Villata M. et al., 1997, A&AS, 121, 119

Villata M. et al., 2002, Mem. Soc. Astron. Ital., 73, 1191

Villata M. et al., 2009, A&A, 504, L9

Villata M., Raiteri C. M., 1999, A&A, 347, 30

Vovk I., Neronov A., 2013, ApJ, 767, 103

Wang J.-Y., An T., Baan W. A., Lu X.-L., 2014, MNRAS, 443, 58

Witt A., Schumann A. Y., 2005, Nonlinear Process Geophys., 12, 345

Zhang P.-f., Yan D.-h., Liao N.-h., Wang J.-c., 2017a, ApJ, 835, 260

Zhang P.-F., Yan D.-H., Zhou J.-N., Fan Y.-Z., Wang J.-C., Zhang L., 2017b, ApJ, 845, 82

APPENDIX A: OPTICAL V BAND ANALYSIS FOR 3C 66A

The search for periodicity in 3C 66A was also carried out in the V band in addition to the R band presented in Sections 4.1.1 and 4.1.2. Fig. A1 shows the results for the total optical magnitude. The ZDCF exhibits a periodic structure with maxima/minima reaching a CL of 2σ–3σ. The period derived from the ZDCF is 2.04 ± 0.10 yr. The LS periodogram presents a peak at a CL of $\sim 2\sigma$ with a period of 2.48 ± 0.29 yr. The available data in V-band cover only the low state period of the R-band light curve, so this result is comparable to the R-band result for this period. Peaks with lower periods at a CL of $\sim 2\sigma$ appear due to the gaps in the coverage and uneven sampling of the light curve. Finally, a peak is identified in the WWZ diagram with a period of 2.28 ± 0.47 yr and at a significance of $\sim 3\sigma$.
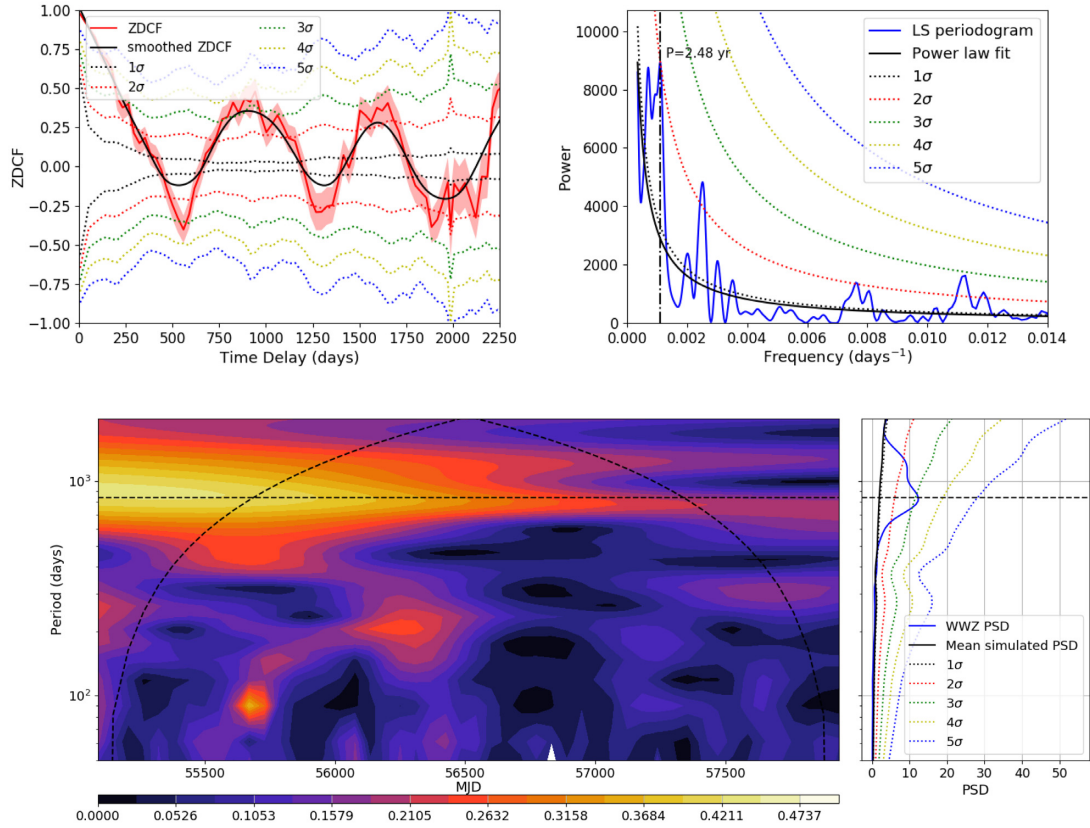
Figure A1. Periodicity analysis of the *V*-band data of 3C 66A. *Top left*: ZDCF method. The autocorrelation is given in red and the smoothed curve in black. *Top right*: Lomb–Scargle periodogram. The periodogram is given in blue and the power-law fit in black. *Bottom*: WWZ diagram. The left-hand panel shows the 2D power spectrum as a function of period and time. The black-dashed curve represents the COI. The right-hand panel shows the PSD in blue and the mean simulated PSD in black. The coloured-dotted lines represent the different significance levels. The black horizontal dashed line marks the peak of the PSD.

This paper has been typeset from a TEX/LATEX file prepared by the author.